MSci Project Report:
Geolocating the Position of a Volcano on an Extrasolar Planet.

J. Lindsey[*]

University of Birmingham

jxl528@bham.ac.uk

A. Triaud[†]

University of Birmingham

a.triaud@bham.ac.uk

B. Chaplin[‡]

University of Birmingham

w.j.chaplin@bham.ac.uk

March 23, 2018

Approximate Word Count ≈ 8767

Abstract

The motivation of this research is to determine whether the established eclipse slicing method of mapping distant extrasolar gas giants can be applied to resolving volcanic hotspots on terrestrial planets. By building an algorithm from first principles based on TRAPPIST-1b, three models with varying limb-darkening effects and surface features were sliced to simulate a secondary eclipse. By overplotting the resulting lightcurves, residuals demonstrate how the lightcurves vary throughout the ingress and egress stages for each model. Utilising an estimated SNR for the JWST from Spitzer measurements with 20 integrated occultations, noisy data was simulated for the volcano model. By performing a MCMC simulation on the three parameters T_{tot}, T_{full} and ΔT, the null hypothesis can only be rejected for ΔT at the 2σ level. To test the impact of an eccentric orbit, the variation in each sampled parameter was plotted against ω, the argument of periapsis. It was found that the uncertanties were too large for T_{tot} and T_{full}, with ΔT being discernable from an eccentric orbit at the 1σ level, assuming eccentricity can be constrained via another method. This suggests ≈ 200 occultations are necessary to obtain a 3σ detection, which opposes the requirement that the smallest number of occultations are used due to the rapid variability of surface volcanoes. Furthermore, it is estimated that a telescope with diameter $\approx 25m$ is necessary to obtain the same MCMC results within a single occultation.

---
[*]Student ID: 1428926
[†]Lead Project Supervisor
[‡]Project Supervisor

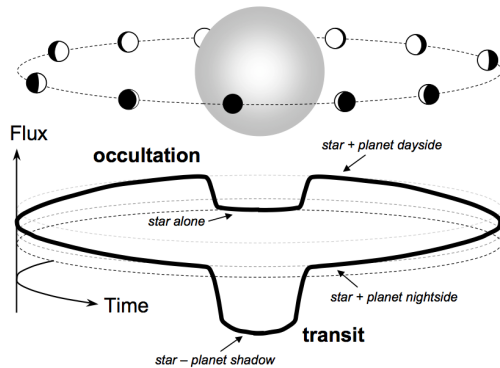# CONTENTS

1. INTRODUCTION

Figure 1: *Visual representation of the various phases throughout an exoplanet's orbit. The flux varies throughout the full orbit, with two distinct drops; the transit and occultation. To an observer, the exoplanet's day-side is visible immediately before and after an occultation, with any rotation of the planet assumed to be negligible.*
(Credit: Winn (2010))

1.1. Motivation:

Transiting exoplanets, those which orbit a star other than our own, have potential to provide a significant amount of information regarding their astronomical properties (Winn (2010)). As an exoplanet crosses the path of its host star, it eclipses the stellar light, and a decrease in flux is detected from the system defined as a *primary eclipse*. An exoplanet may also traverse behind the star, which is defined as a *secondary eclipse* (see figure 1). In the case of an exoplanet becoming totally obscured, this is called an *occultation*, with partial obscurity or *grazing* to include the case where a total eclipse does not occur. If the viewer happens to be in a position that observes a primary transit, it becomes possible to infer numerous properties,

such as the size ratio between an exoplanet and its star. This can be advanced by analysing atmospheric properties with transit-transmission (de Wit et al. (2012)). However, the system is detectable only as a point source, which necessitates additional techniques to extract further information, such as the spatial variation of flux on the exoplanet's surface.

The powerful eclipse mapping technique bridges the gap between detecting an occultation and resolving spatial features on an exoplanet's surface. This has already been applied to Jupiter-sized planets (specifically HD189733b) allowing off-centred hotspots to be located (Majeau et al. (2012)) and for various photospheric emission models to be resolved (Rauscher et al. (2007)). The technique is yet to be applied to a terrestrial planet with different hotspot-forming mechanisms to a Hot Jupiter. The previous research applied to HD189733b suggests supersonic winds may be present causing a hotspot shift from the sub-stellar point (Knutson et al. (2007)), but the mechanism may differ for a similar hotspot on a terrestrial planet. Magnetic induction and tidal forces may generate volcanic activity, potentially leading to the release of greenhouse gases into the atmosphere (Kislyakova et al. (2017)). It is the aim if this study to determine if a surface feature generated by a volcano is detectable with the eclipse mapping technique.

1.2. Aims:

The specific aims of this study are:

1. To model the TRAPPIST-1b exoplanet with varying levels of limb-darkening and a volcano-generated hotspot.
2. To model the eclipse-mapping technique to obtain various lightcurves with corre-

sponding reconstructed images.

3. To employ a Monte-Carlo simulation to determine the confidence level at which the volcano can be detected with a signal-to-noise ratio comparable with the James Webb Space Telescope.

4. To determine if this detection is degenerate with an eccentric orbit, and if this degeneracy can be lifted.

2. Theory

2.1. Eclipse Mapping:

By measuring the loss in flux shortly before and after an exoplanet becomes fully occulted during the secondary eclipse, it is possible to determine a full disk-integrated flux value (Winn (2010)), but with no spatial information being provided. However, by employing additional knowledge regarding the exoplanet system, the lightcurve shape during partial-occultation becomes valuable. As an orbiting body begins traversing behind its star, the *ingress* phase, the resulting lightcurve shape varies depending on the body's brightness distribution (BD) (Knutson et al. (2007)). Similarly, this occurs as the body is revealed a short time later, which is the *egress* phase. By dividing the ingress and egress phases into an arbitrary number of temporal slices, it is possible to obtain integrated flux measurements which represent spatial slices of the orbiting body's BD (Majeau et al. (2012)). This provides us with with a one-dimensional interpretation of the BD on the body's surface. However, if the orbiting body is occulted with a non-zero impact parameter b, defined as the distance from the stellar equator often measured in units of solar radius R_S, the orbiting body is 'sliced' at a non-

vertical angle (de Wit et al. (2012)). This enables a two-dimensional map to be created, and this process is termed eclipse mapping (see figure 2). If N slices are taken during both the ingress and egress, then N^2 segments will be present in the final image. It is therefore beneficial for the largest number of possible slices to be measured allowing an increased final resolution. In the past, this eclipse mapping technique has been applied to stellar binaries (Majeau et al. (2012)), but in this study these techniques will for the first time be applied to a terrestrial exoplanet. The creation of the two-dimensional map in figure 2 can sometimes lead to the assumption that the intensity distribution on the planet's surface varies smoothly (Majeau et al. (2012)), allowing a linear regularisation term to enforce small changes in neighbouring pixels (Knutson et al. (2007)). This may introduce uncertainties with random and discreet surface features such as volcanoes, and therefore the imposition of linear regularisation was not considered reasonable in this study.

2.2. Summary of Past Research:

This research is not the first to use the eclipse mapping technique, which has already been applied to exoplanets on several occasions. First introduced by Williams et al. (2006), the *uniform time offset* measures the time delay between the centre of an observed occultation and that expected by an equivalent exoplanet with a uniform BD. If a planet displays an intensity distribution where the brightest region is shifted left/right of the sub-stellar point, the resultant shape of the ingress and egress will not be identical, with the full occultation lightcurve appearing shifted in phase. This was confirmed by Knutson et al. (2007), which
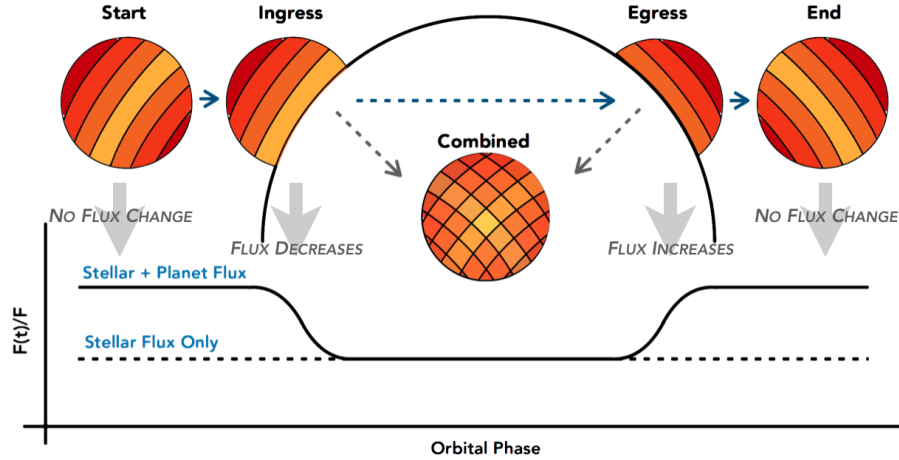
Figure 2: *Top: Demonstration of the eclipse mapping technique. Each image (from left to right) presents the exoplanet progressing through the secondary eclipse. During the ingress, several slices are taken at an angle depending on the impact parameter, and is repeated during the egress. The combined map in the centre is then generated. Geographical information can only be collected during the ingress/egress stages.*

Bottom: Example lightcurve which represents what an observer would detect at each stage. The change in total star-planet flux provides us with the necessary information to create the combined map.

(Modified from: Majeau et al. (2012), also used in poster: Lindsey (2018))

detected a time offset of ≈ 120 seconds on the Hot Jupiter HD189733b. This was suspected to be caused by both an eccentric orbit (see section 2.4 figure 5) and a off-centred hotspot with equatorial latitude. Knutson created a one-dimensional low-resolution map with linear regularisation and no limb-darkening, but a two-dimensional representation was not formally tested. A simulated form of eclipse mapping by Rauscher et al. (2007) then applied this technique to various photospheric emission models of HD189733b. This procedure generated ingress/egress curves and applied noisy measurements for both Spitzer and the James Webb Space Telescope (JWST). Whilst Spitzer was found to be insufficient in distinguishing between the emission models in many of the cases presented by Rauscher, JWST's results proved to be promising, and will therefore become a fundamental part of this study.

Rauscher did not adopt flux limb-darkening in their research, but it was discussed whether a simple radially-dependent cosine law could be adopted. A decrease in temperature was instead implemented in a $\cos^{\frac{1}{4}}(\phi)$ form. Albedo, the measure of incident solar radiation which is scattered back in space, can potentially influence any occultation model, but Rauscher found that small variations in the albedo had a minimal change on their final results, but this will be examined in section 3.2. Furthermore, Rauscher listed two possible emission models: a simple blackbody Planck function approximation, and a grid of atmospheric spectral models over a range of temperatures. The results differed depending on the model used, but not to a significant degree. As a result, the blackbody model will be implemented as a crude approximation in an effort to save research time.

5

Following this, Majeau et al. (2012) created the first secondary-eclipse map of HD189733b adopting Spitzer $8\mu m$ IRAC data, which presented an off-centred hotspot from the substellar point. Majeau implemented both eclipse mapping by slicing and spherical-harmonics, with advantages to both techniques. Most notably, the spherical-harmonic approach is able to utilise a full orbital period, whereas the slicing approach is constrained to only the ingress/egress portions of the orbit. However, slicing can extract latitudinal information with a non-zero impact parameter, leading to a static brightness map if it is assumed the rotation of the planet is negligible throughout the duration of an occultation. This is not the case for spherical-harmonics over a full phase, but a static map is important for a volcanic detection (see section 2.3). Furthermore, slicing has no theoretical resolution limit, which increases with the number of slices obtained during ingress/egress. However, the technique is limited by the north-south degeneracy, where it is not possible to know if the exoplanet's orbital angular momentum vector is pointed towards/away from an observer. It is therefore not possible to state if a volcano or surface feature is present in the northern/southern hemisphere, even if the exoplanet is occulted with a non-zero impact parameter. A similar analysis was performed by de Wit et al. (2012), which linked the offset on HD189733b's surface to eccentricity, stellar density and the impact parameter. de Wit also noted the importance of a non-zero impact parameter to collect two-dimensional information on the Hot Jupiter's surface. However, this analysis differed from Majeau et al. (2012) in several ways, such as constraints not being imposed a priori. The orbital eccentricity was not restricted to

be zero, and further parameters were shown to be directly linked to eclipse mapping beyond an exoplanet's BD. de Wit also rejects an oblate-shaped exoplanet, instead preferring a non-uniform BD, where both can introduce a uniform-time offset.

2.3. TRAPPIST-1b:

As the eclipse mapping technique measures fractional change in flux from the combined star-planet system, it is beneficial to select a smaller star as this leads to a greater variation in combined flux throughout a secondary eclipse (Winn (2010)), hence an improved signal-to-noise ratio (SNR). Furthermore, as it is intended to advance the eclipse mapping technique to volcanic hotspots, a terrestrial planet would be best suited. The TRAPPIST-1 (T1) system was selected on these criteria (Gillon et al. (2017)), specifically TRAPPIST-1b (T1b), due to the host star being an ultra-cool red dwarf and the exoplanet being terrestrial with mass and size properties similar to Earth (see table 1 for parameters), a thoroughly-studied planet. The T1 system consists of seven transiting exoplanets, all of which orbit within 0.1AU of their host star. The system itself is located 12pc from Earth (Luger et al. (2017)), with planet-planet occultations (PPOs) occurring - where occultations between two planets are detected without passing behind the host star. This enables both the day *and* night-side to be investigated depending on the PPO location. If T1b possesses a small but non-zero eccentricity, it is likely that tidal disruptions can heat the material in the upper-mantle, potentially leading to volcanic activity (Gaidos & Nimmo (2000), de Kleer & de Pater (2016)). This may also be possible via electromagnetic

Table 1: *Values used for the TRAPPIST-1b exoplanet. All values originate from Gillon et al. (2017) unless denoted with [*], which utilise updated values by Grimm et al. (2018) along with the smallest errors from all TRAPPIST-1 planets, which may optimistically be obtainable in future observations.*

Parameter	Value with Errors
Stellar Radius R_S ($R_\odot$)	0.117 ± 0.0036
Radius R_P (R_{Earth})	1.086 ± 0.035
Semi-major Axis a (10^{-3}AU)	11.11 ± 0.34
Inclination i ($°$)	$89.65^{+0.22}_{-0.27}$
Impact Parameter b (R_S)	$0.126^{+0.092}_{-0.078}$
Scale Parameter $\frac{a}{R_S}$	$20.50^{+0.16}_{-0.31}$
Period P (d)	$1.51087081 \pm 0.60 \times 10^{-6}$
Transit Duration T (min)	36.40 ± 0.17
Eccentricity e	0.00622 ± 0.00058 [*]
Equilibrium Temp T_{eq} (K)	400.1 ± 7.7
Stellar Temp T_S (K)	2559 ± 50
Arg of Periapsis ω ($°$)	336.86 ± 3.11 [*]

inducing heating caused by the planet's orbital motion (Kislyakova et al. (2017)), leading to the development of magma oceans. Surface volcanoes have been directly observed in the near infrared on Jupiter's moon Io over a period of 100 days (de Kleer & de Pater (2016)). During this time, the large eruptions were observed to rapidly vary within a few hours, with the power output varying over several orders of magnitude within a few days (de Kleer & de Pater (2016)). As a result of this, it is preferable for information to be obtained during a single occultation, as the surface features may have varied before a second occultation is observed. This may not be feasible with JWST, necessitating multiple occultations to obtain a detectable SNR. If this scenario is unavoidable, it is also important that T1b is likely tidally-locked (orbital period $\approx$ rotational period) (Gillon et al. (2017)), such that the side of the planet facing us during an occultation does not change over

multiple orbits, enabling the same surface features to be mapped. As T1b is a terrestrial planet with Earth-like properties, it will be assumed to exhibit an albedo of $\approx$0.3 (Stephens et al. (2012)) as a simple approximation. However, as discovered by Rauscher et al. (2007), modifying the experimental albedo from 0 to 0.3 made little difference on their final results, and so this value will not be modified throughout the procedure.

2.4. Orbital Parameters:

Any model created in section 3 will use several orbital parameters to replicate what might be expected from the T1b system. The first of these is orbital phase, and these parameters are illustrated in figure 3. Here, b is the impact parameter, τ is the ingress/egress time, t_{I-IV} describes the four points of contact, with $t_{I,IV}$ being the points of first and last contact
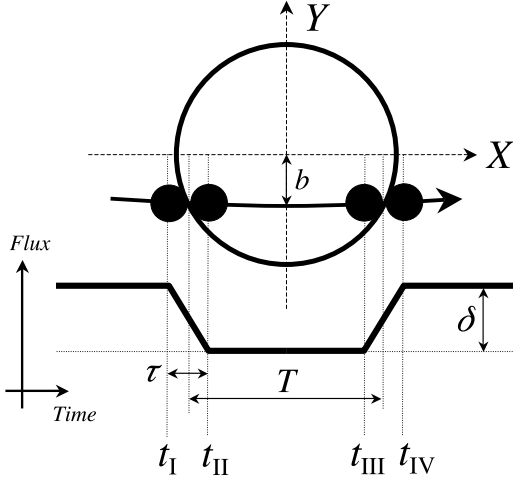
Figure 3: *Illustration of an orbital transit/occultation, with a planet passing in-front/behind the star from left-right. The parameters τ, T, t_{I-IV}, δ and b are detailed in section 2.4. The coordinate system is centred on the star, with an observer placed on the Z-axis.*
(Credit: Winn (2010))

Figure 4: *Orbital diagram with the longitude of the ascending node Ω, argument of periapsis ω and inclination i labelled. In this case, the ascending node is not aligned along the X-axis, causing the planet to be misaligned with its host star (assuming the star is aligned along the Y-axis). The coordinate system is centred on the star, with an observer placed on the Z-axis.*
(Credit: Murray & Correia (2010))

of the occultation and $t_{II,III}$ representing the points where the planet is fully occulted. Furthermore, δ is the occultation depth and T is the time between mid-ingress and mid-egress. From this, there are two key parameters which can be extracted: T_{tot} and T_{full}. The first parameter represents the total occultation time, defined as $T_{tot} = t_{IV} - t_I$. The second parameter describes the fully-occulted time of the planet, with no region of the surface being visible and no information being used, defined as $T_{full} = t_{III} - t_{II}$. For a circular orbit, it is possible to measure both the total occultation and fully-occulted times by (Winn (2010)):

$$T_{tot} = \frac{P}{\pi} \sin^{-1}\left(\frac{R_S}{a} \frac{\sqrt{(1+k)^2 - b^2}}{sin(i)} \right) \quad (1)$$

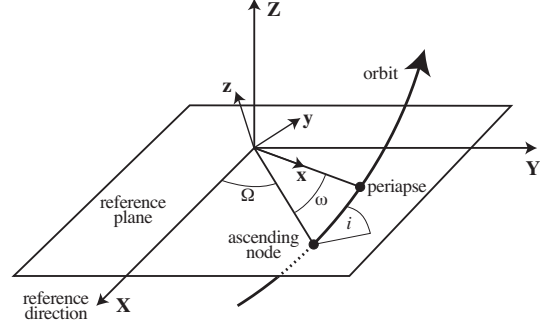$$T_{full} = \frac{P}{\pi} \sin^{-1}\left(\frac{R_S}{a} \frac{\sqrt{(1-k)^2 - b^2}}{sin(i)} \right) \quad (2)$$

where k is defined as the ratio of planetary and stellar radius $\frac{R_P}{R_S}$. All other parameters are defined in table 1. The ratio $\frac{a}{R_S}$ is often called the scale parameter, and is a quantity that is directly observed from the exoplanet system using T_{tot} and T_{full} (see equation (27) by Winn (2010)). From this, the ingress/egress time can be determined via

$$\tau = \frac{\left(T_{tot} - T_{full} \right)}{2}, \quad (3)$$

for zero eccentricity. If the orbit is non-circular, equations (1) and (2) can be modifying by the multiplicative factor

$$\frac{\sqrt{1 - e^2}}{1 - e \sin \omega} \quad (4)$$

where e is the orbital eccentricity and ω is the *argument of periapsis*. This is defined as the angle between the periapsis (closest approach to

the star) and the ascending node of the orbit. If the ascending node is placed along the X-axis in figures 3 and 4 ($\Omega = 0°$ or $180°$), ω is measured from the X-axis to the orbital periapsis in the X-Z plane with inclination = $90°$. In the case that the ascending node does not align with the X-axis, or inclination $\neq 90°$, the planet will be spin-orbit misaligned with its host star (which is assumed aligned with the Y-axis). However, the alignment of the star is not relevant to the slice eclipse mapping technique, and so the ascending node will be assumed to lie on the X-axis. This assumption and notation follows that used by Winn (2010), with further information available by Murray & Correia (2010).

For non-circular orbits, the impact parameter b also differs between the transit and occultation, as the star-planet distance will vary throughout an orbit. Taking the key equation from Winn (2010)

$$b_{occ} = \frac{a\cos(i)}{R_S}\left(\frac{1 - e^2}{1 - e\sin(\omega)}\right), \qquad (5)$$

and using all previously defined parameters, it is possible to find the impact parameter at conjunction (X=0 in figure 3). Furthermore, the time difference between the transit and occultation conjunction is defined by (Winn et al. (2007), Winn (2010), de Wit et al. (2012))

$$\Delta T \approx \frac{P}{2}\left[1 + \frac{4}{\pi}e\cos\omega\right], \qquad (6)$$

which depends specifically on $e\cos(\omega)$ and reduces to $\frac{P}{2}$ for a circular orbit (see figure 5 for visualisation).

3. METHOD

By utilising the theory set out in section 2, a model was built from first principles to
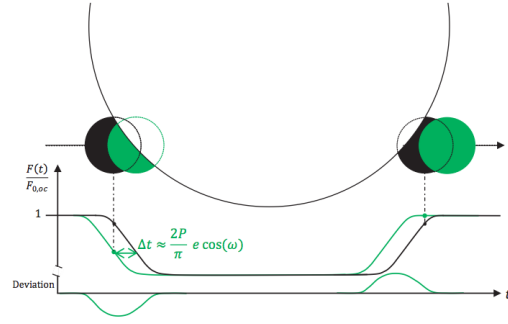

Figure 5: *Schematic representation showing the effect of an eccentric orbit ($e\cos(\omega)$) on the timing of occultation.*
(Credit: de Wit (2014))

combine the previous research on HD189733b and apply this to TRAPPIST-1b. It is not yet possible to directly detect volcanoes outside our solar system, so it is necessary to construct a model planet, followed by the simulation of an occultation to obtain a lightcurve. This simulation has been coded entirely in `Python 2.7` using a combination of `Jupyter Notebooks` and `Python` files. A copy of these files can be found on the `Github (Username: "jlindsey1")` repository.

3.1. Building the Model:

3.1.1 Generating Planets:

Three simple models have been chosen to replicate the eclipse mapping technique:

- A non-limb-darkened disk. This models the uniformly-bright disk tested by de Wit et al. (2012).
- A cosine limb-darkened planet, mirroring the application by Rauscher et al. (2007), but with flux rather than temperature variation. This model is the "null hypothesis".
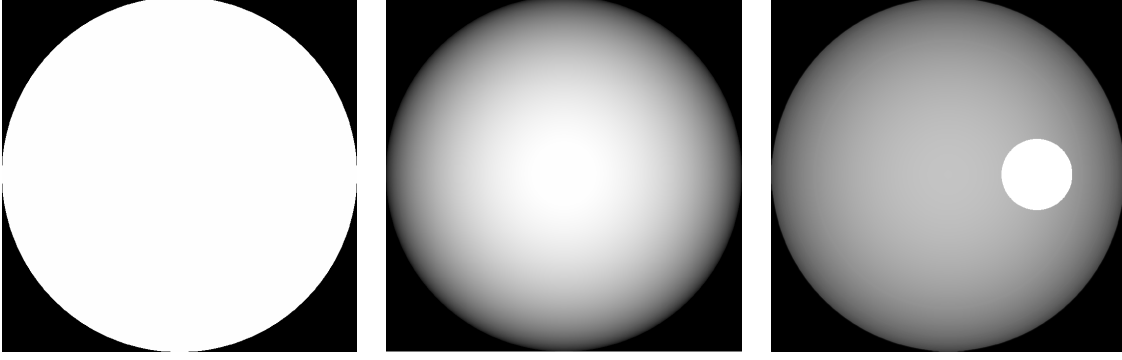- A planet with a surface feature, along

Figure 6: *Illustration of the three generated models, situated on the X-Y plane. Left: uniformly-bright planet. Centre: cosine limb-darkened planet. Right: combined limb-darkened planet with added surface feature, $N_{ratio} = 0.1$ in this example. The total integrated flux within each generated model is equal. Each image is a visualised `".fits"` array using `SAOImage DS9`.*

with cosine limb-darkening. The model-generating code will be able to modify the shape, location and intensity of the feature.
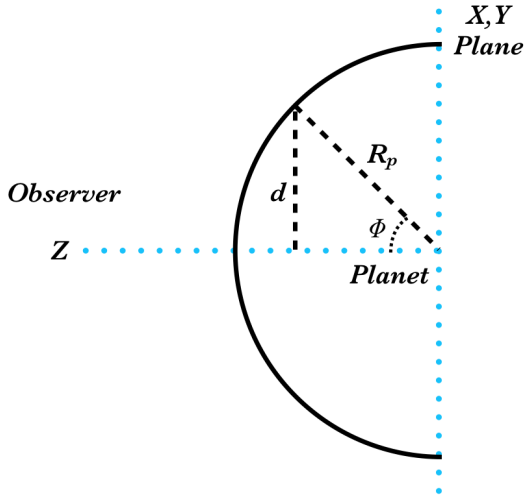

Figure 7: *Diagram of planet linking ϕ, d and R_P, with an observer on the Z-axis. This is discussed in section 3.1.1*

Visual illustrations of these models are presented in figure 6, with the volcano/feature model exhibiting a flux ratio of 0.1. This is

defined as

$$N_{ratio} = \frac{F_{feature}}{F_{total}}, \qquad (7)$$

thus a ratio of 0.1 translates to 10% of total flux contained. Equivalently, $N_{ratio} = 1.0$ would describe a feature with 100% of the planet's flux.

The illustrations in figure 6 represent two-dimensional 1500×1500 `NumPy` arrays, with each pixel containing only a number to represent flux. The dimensions are arbitrarily chosen with a high resolution, but can be varied as necessary. The pixel value is also arbitrary, representing only the flux variation across the array, and is translated into a meaningful value for T1b in section 3.2. Limb-darkening is applied via a cosine-law from the sub-stellar point, $\cos(\phi)$, where the angular distance ϕ is determined by

$$\phi = \sin^{-1}\left(\frac{d}{R_P}\right), \qquad (8)$$

where d is the linear distance from the sub-stellar Z-axis to a position on the surface. In the two-dimensional arrays, only linear distance

d can be used, with equation (8) allowing the angular distance ϕ to be determined. This is visualised in figure 7. The limb-darkening of the planet is not modified between ingress and egress as the rotation of the planet is assumed to be negligible throughout occultation.
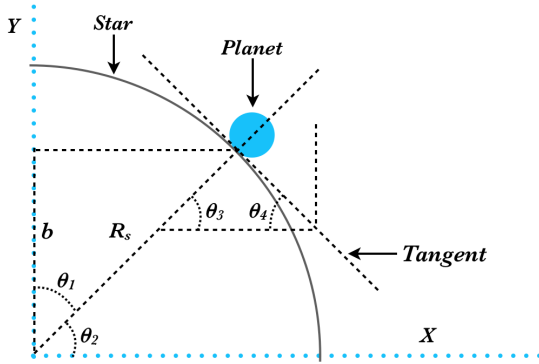
3.1.2 Slicing Method:

Figure 8: *Schematic diagram of a planet immediately before/after an occultation (orbiting on the X-axis), grazing the surface of its host star. Known is the impact parameter b and the stellar radius R_S. Unknown is the tangential angle to the direction of orbit, $\theta_{tangent} \equiv \theta_4$. Derivation in section 3.1.2.*

At this stage, it is required to simulate the ingress/egress to construct an occultation lightcurve. Four assumptions will be made in order to simplify the necessary code:

1. $R_P \ll R_S$: By assuming the planet is much smaller than the star, the occultation segments can be approximated as straight rather than curved. Using values from section 2.3, $k = \frac{R_P}{R_S} \approx 0.085$, which is $\ll 1$.
2. $R_S \ll a$: This allows the planet's path across its star to be approximated as a straight line (Winn (2010)). Using T1b values, the inverse scale parameter $\frac{R_S}{a} \approx 0.049 \ll 1$.

3. $e = 0$: A circular orbit will be assumed, with the impact of an eccentric orbit introduced at a later stage in section 3.7.
4. *Orbital Direction*: The planet will be assumed to occult from right-left in figure 3 so that slices will be removed starting from the planet's left side.

By combining point 2 with the assumption that the ascending node is aligned with the X-axis (section 2.4, figures 3 and 4), the planet traverses behind the star in a straight horizontal line. This results in the angle of slicing, $\theta_{tangent}$, being unchanged between ingress and egress. Using these assumptions, each model in figure 6 can now be sliced into segments.

To determine the slicing angle, a schematic is presented in figure 8. Of the four angles θ_{1-4}, the angle linking the stellar tangent to the orbital direction (X-axis) is $\theta_{tangent} \equiv \theta_4$. To determine this angle, equations (9) - (12) can be used, directly derived from figure 8.

$$\theta_1 = \frac{\pi}{2} - \theta_2 \qquad (9)$$

$$\theta_3 = \frac{\pi}{2} - \theta_4 \qquad (10)$$

$$\theta_2 = \theta_3 \qquad (11)$$

$$\therefore \theta_{tangent} \equiv \theta_4 = \theta_1 \qquad (12)$$

Furthermore, the right-angled triangle linking b, R_S and θ_1 can be used to state

$$\theta_{tangent} = \theta_1 = \cos^{-1}(b_{occ}), \qquad (13)$$

noting that b_{occ} has dimensions of *stellar radius*. If utilising *SI units*, then an additional factor of R_S would be necessary within the $\cos^{-1}$ denominator in equation (13). Using the impact parameter for T1b from table 1, the slicing angle can be found.
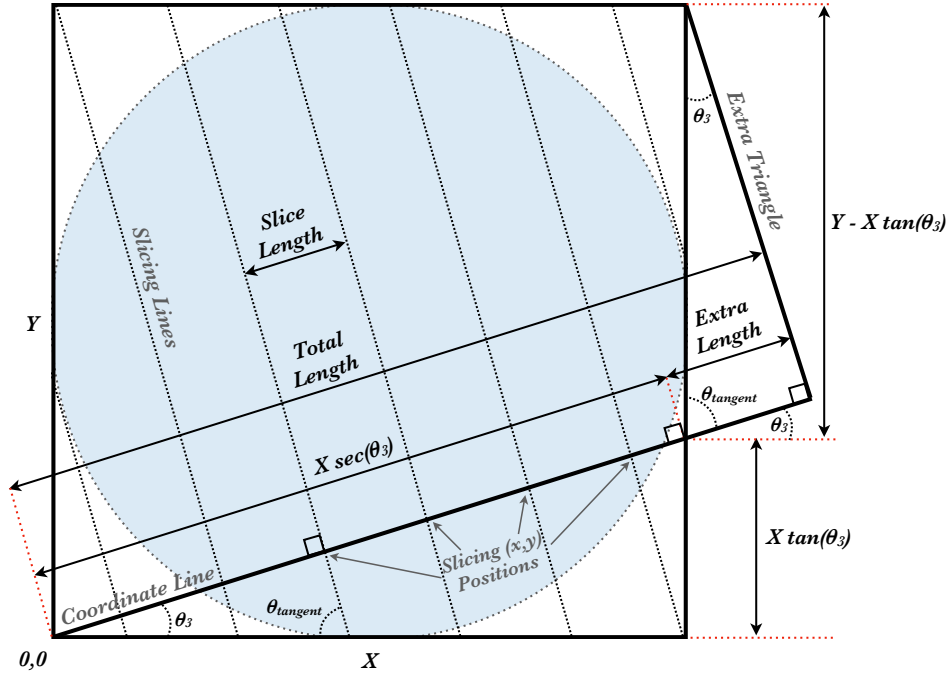
Figure 9: *Schematic diagram to represent the calculations used to slice the model planets. The "coordinate line" represents where the "slicing lines" are drawn from within the Python code. Using trigonometry in section 3.1.2, the "slicing positions" are calculated, which allows the "slicing lines" to be drawn.*
For $\theta_{tangent} \neq \frac{\pi}{2}$, the total length must extend beyond the image border to ensure the slices encompass the upper-right corner, allowing the "slicing lines" to extend beyond $X\sec(\theta_3)$.

Following the calculation of the slicing angle, which is equal-but-opposite between ingress and egress following previously made assumptions, the model planets must now be segmented. If the planet is occulted along the stellar equator, the model image would simply be sliced into vertical segments. In the case of T1b, however, the impact parameter is non-zero, and so the slicing must occur at an angle, visualised in figure 9. This shows the geometry of the slicing method, with the following equations being derivable:

$$L_{extra} = (Y - X\tan(\theta_3))\cos(\theta_{tangent}) \quad (14)$$

$$L_{total} = X\sec(\theta_3) + L_{extra} \quad (15)$$

$$L_{slice} = \frac{L_{total}}{N_{slices}} \quad (16)$$

To expand upon this:

- $\theta_{tangent}$ and θ_3: These are known for the system, and are calculated in equations (10), (12) and (13).
- X, Y: These are the input dimensions of the model planet.
- *Extra Length* L_{extra}: This is calculated from equation (14). In the case that $\theta_{tangent} = \frac{\pi}{2}$, this simplifies simply to *zero*.
- *Total Length* L_{total}: This is the total length

which must be considered when determining the size of each slice, and is calculated in equation (15). In the case that $\theta_{tangent} = \frac{\pi}{2}$, this simplifies simply to X.

- *Slice Length L_{slice}*: This is the key parameter to plot the slices and divide the model planet. This is determined in equation (16), and depends on the number of input slices N_{slices}.

Once the length of each slice is known, the lines separating each slice in figure 9 can be plotted. The (x, y) coordinates (calculated in section A.1) to locate each line positioned along the *"Coordinate Line"* can be calculated. These positions are the *"Slicing Positions"*, with a slice segment then drawn at an angle $\theta_{tangent}$. Using this, it is then possible to link the impact parameter of T1b and the radius of its host star to the coordinates of each individual slice in the generated model planets. By employing these equations for an example of $N_{slices} = 50$, the sliced ingress phase is presented in figure 10, with the equivalent egress in figure 26 (section A.5).

3.2. Applying to TRAPPIST-1b:

Once the occultation has been simulated, it is necessary to apply the physical parameters of the T1b system. This requires knowledge of orbital timing along with flux approximations.

3.2.1 Calculating Phase:

To estimate the phase timings, for a circular orbit, equations (1) and (2) are utilised to determine the time between the four points of contact, t_{I-IV}. From this, two arrays can be generated, each with length N_{slices}, ranging from:

- Ingress: $\left[\frac{P}{2} - \frac{T_{tot}}{2}, \frac{P}{2} - \frac{T_{full}}{2} \right]$
- Egress: $\left[\frac{P}{2} + \frac{T_{full}}{2}, \frac{P}{2} + \frac{T_{tot}}{2} \right]$

This assumes the midpoint of the occultation occurs at $\Delta T = \frac{P}{2}$ for a circular orbit (see section 2.4), and the ingress/egress duration τ follows equation (3).

3.2.2 Calculating Flux:

The ingress lightcurve in figure 10 displays an arbitrary flux scale on the Y-axis, not specific to any exoplanet. This stems from the pixel value assigned to each of the three model planets generated, but these values are used only to hold information regarding the BD and how this varies across the surface. The Y-axis in figure 10 can be corrected for T1b by normalising to the host star. As discussed in section 2.2, Rauscher et al. (2007) utilised two possible emission models for Hot Jupiter HD189733b, one being a simple blackbody Planck function. Radiation from the T1b system originates from both thermal radiation and starlight which has been reflected (Winn (2010)). As this study aims to determine if a volcano-generated hotspot is detectable on an 'order-of-magnitude' scale, the Planck function will be sufficient to obtain an estimation for the planet-star flux values.

The Planck function for wavelength λ at a given temperature T is given by (Winn (2010))

$$B_\lambda = \frac{2hc^2}{\lambda^5} \frac{1}{\exp(\frac{hc}{\lambda kT}) - 1}, \qquad (17)$$

where all constants have their usual meaning. This is a measure of a body's spectral radiance for a given wavelength and temperature. Consequently, if the stellar and planetary temperatures are known, their spectral radiance can be plotted with wavelength, allowing an optimal wavelength to be chosen to normalise
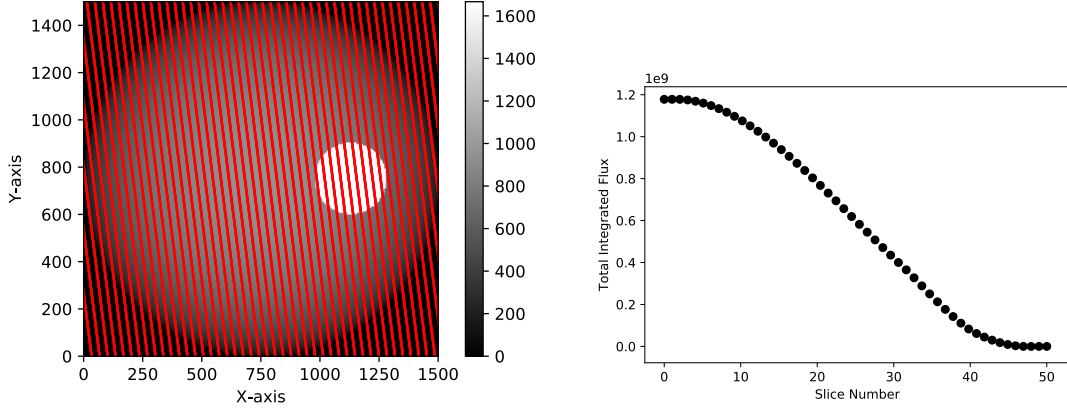
Figure 10: *Result of the slicing method described in section 3.1.2. Left: ingress phase. Right: resultant lightcurve. The lightcurve is simulated by progressively removing individual slices from the segmented model. Each slice is deducted from the total integrated flux to replicate an opaque star eclipsing the planet. This simulated lightcurve then contains one-dimensional information of the planet's brightness distribution.*

figure 10. To estimate the planet's temperature, a uniform heat-redistribution model has been assumed (Rauscher et al. (2007)) where the equilibrium temperature can be estimated (from Seager et al. (2009) with a different redistribution model) by

$$T_P = (1 - A)^{\frac{1}{4}} \frac{T_S}{\sqrt{2}} \left(\frac{R_S}{a} \right)^{\frac{1}{2}}, \qquad (18)$$

where A is albedo and all other values are listed in table 1. This can be derived by equating the stellar and planetary luminosity, and noting that the fractional absorbed luminosity impacting the planet's surface is

$$L_{P,absorbed} \propto (1 - A) \left(\frac{R_P}{2a} \right)^2 L_S. \qquad (19)$$

This can be converted to temperature using $L \propto T^4$ (Seager et al. (2009)). Likewise, the reflected luminosity is (Winn (2010))

$$L_{P,reflected} \quad \propto \quad 1 - L_{P,absorbed}, \qquad (20)$$

$$L_{P,reflected} \quad \propto \quad A \left(\frac{R_P}{2a} \right)^2 L_S. \qquad (21)$$

The use of equation (18) is not necessary if the temperature is known via other means, and in the case of T1b, a value of $T_P = 600K$ (Triaud Private Communication (2017)) will be favoured.
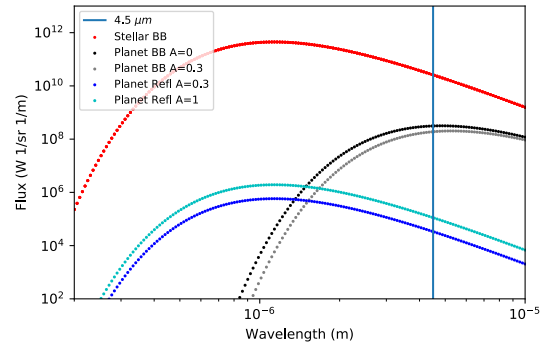

Figure 11: *Plotted Planck function for T1 and T1b for reflected and thermal (BB blackbody) emission with varying albedo values. Also noted is $\lambda = 4.5\mu m$, which is the infrared Spitzer band.*

Presented in figure 11 is a blackbody plot for T1b and its host star, aiming to replicate Seager & Deming (2010) with the use of equation 17. The value of $A = 0.3$ is adopted for T1b (see

section 2.3). A wavelength value of $\lambda = 4.5\mu m$ is selected to both replicate the Spitzer measurements to allow SNR scaling in section 3.5, in conjunction with exhibiting an optimal star-planet contrast. It is noted that the planet's thermal emission is present at a longer wavelength to the reflected starlight, which is due to the planet's cooler surface temperature (Winn (2010)). As a surface volcano will generate light rather than reflect starlight, the $4.5\mu m$ band conforms to this requirement. By noting the stellar and planetary flux at this wavelength, it is possible to estimate the stellar flux adapted to the generated model planets, $F_{S,Model}$, using

$$F_{S,Model} = \frac{F_{S,BB}R_S^2}{(F_{P,BB} + F_{P,R})R_P^2}F_{P,Model},\quad (22)$$

where R_P/R_S is the radius of the planet/star, $F_{P,Model}$ is the total integrated flux from the model, $F_{S,BB}$ represents the estimated stellar flux and $F_{P,BB}/F_{P,R}$ is the estimated planetary thermal/reflected flux respectively. At this stage, the values in figure 10 can be normalised to $F_{S,Model}$ to complete the T1b model replication. In a true observation, the flux of the star may vary during an occultation, but this could be rectified by measuring and normalising to this stellar variation.

3.2.3 Plotting the Lightcurve:

By combining the phase measurements (section 3.2.1) and flux normalisation (section 3.2.2), it is possible to convert the ingress (and corresponding egress) in figure 10 to a final lightcurve, presented in figure 12. Due to the normalisation process, a flux ratio of $\frac{F(t)}{F} = 1.0$ describes only the host star, with any flux exceeding this incorporating the planet's flux.

3.3. Image Reconstruction:

To extract spatial information from figure 12, it is imperative to note that the flux $F(t)$ at a given time t is proportional to the planets light-distribution function $I(\theta, \phi)$ (from spherical coordinates) integrated over the area of the planet obscured/revealed $A(t)$. This is visualised in figure 13, which follows the notation used by Majeau et al. (2012). By applying this technique and reconstructing the image using the same slicing algorithm used in section 3.1.2, the resulting planet is presented in figure 14.

It is clear from this image that some spatial information has been lost compared to the original volcano model in figure 6, which is a consequence of being constrained to the dimensions of the orbit. T1b's impact parameter results in $\theta_{tangent} \approx \frac{\pi}{2}$, which leads to the ingress and egress reconstruction being almost vertical. In the case that $\theta_{tangent} = \frac{\pi}{2}$, the ingress/egress reconstruction would be identical, only providing us with one-dimensional information. It is therefore preferred that $\theta_{tangent} = \frac{\pi}{4}$ to allow completely different spatial information to be obtained during ingress/egress stages.

3.4. Image Degeneracy:

In the hypothetical case that $\theta_{tangent} = \frac{\pi}{4}$, with T1b's impact parameter being $b \approx 0.71R_S$ (from equation (13)), the slicing would occur at completely opposite angles between ingress/egress.. In this scenario, it was found that some arrangements of initial features would introduce degeneracy in the reconstructed images. Within figure 15, two particular arrangements were compared: a set of four equidistant surface features and a continuous circular feature. The reconstructed images appear visually similar, and without
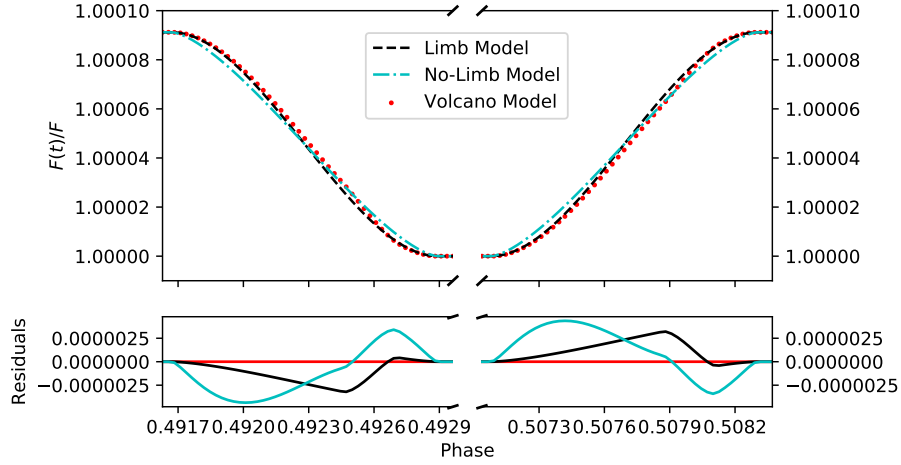
Figure 12: *Final normalised lightcurve from simulated occultations of all three model planets with residuals (compared to the volcano model). As information cannot be obtained when fully occulted, this region has not been plotted. The flux variations of each model contains the spatial information regarding each model's brightness distribution.*

prior knowledge of the feature arrangement, it would be difficult to determine the original BD. On the contrary, by displaying contour plots of the inner-regions for both reconstructed planets, it can be seen that only the circular arrangement increases the light intensity within its borders. This is a consequence of the slicing method averaging flux across an entire segment, with some of the circular feature being caught within each segment. This therefore removes any uncertainty on which original model creates a final reconstructed planet, but this may not be the case for all arrangements. This further reinforces the importance of the impact parameter b, as the plots in figure 15 may dramatically vary for $\theta_{tangent} \neq \frac{\pi}{4}$.

3.5. Applying to JWST:

To determine the significance level at which the model with a volcanic feature can be detected, noisy data can be simulated to replicate a true detection. The JWST, scheduled to launch in

2019 (Ciardi et al. (2017)), is an ideal candidate due to its previous simulated studies related to occultations (eg Rauscher et al. (2007), Luger et al. (2017)). To order-of-magnitude estimate the SNR of JWST, equation (27) by Luger et al. (2017) can be applied, which states

$$SNR_{JWST} = SNR_{Spitzer} \left(\frac{A_{JWST}}{A_{Spitzer}} \right)^{\frac{1}{2}}, \quad (23)$$

where A denotes the telescope collecting-area. This has assumed the throughput between telescopes does not vary, which is not the case in real-world applications. In reality, throughput will depend on the chosen bandpass, wavelength, background level and other telescope parameters. By making this assumption, and using the measurements and parameters for Spitzer and JWST, the values and results are presented in table 2.

It was suggested in section 2.3 that an ideal detection would require a single occultation. However, the Spitzer measurements in table 2
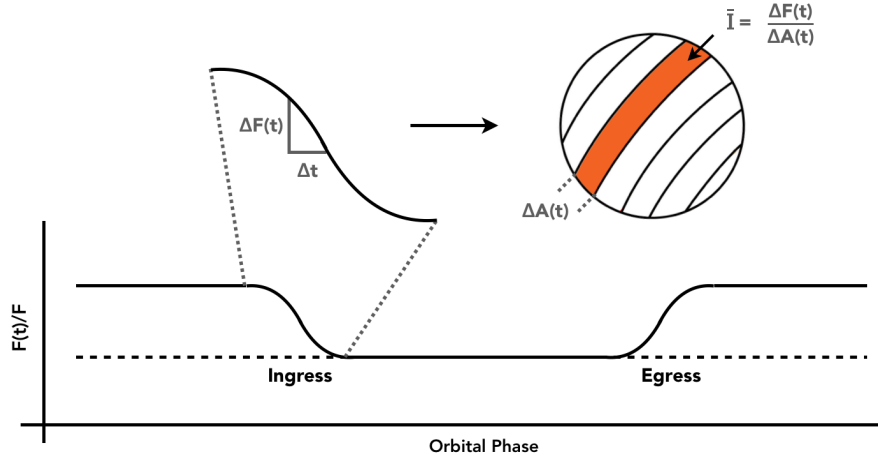
16

Figure 13: *Modified version of figure 2. This demonstrates for the ingress how the extracted flux ΔF for a slice of time t can be averaged across an area ΔA, which provides an average brightness distribution $\bar{I}$ for a given slice on the planet's surface. This can be repeated for the egress if necessary.*
(Modified from: Majeau et al. (2012))

utilise 20 integrated orbits to obtain a SNR of 3. This does introduce an uncertainty that any detected surface feature may not be a volcanic detection, due to the rapid variability of a volcano (de Kleer & de Pater (2016)), and so any results will be scaled to a single occultation in section 4. Now that the SNR for JWST is known for a full occultation curve σ_{Tot}, it must be converted into a standard-deviation for each point σ_{pp} along the curve. This is achieved simply by

$$\sigma_{pp} = \sigma_{Tot}\sqrt{N}, \tag{24}$$

where N is the chosen number of points. This suggests that by increasing the number of points along the lightcurve, simultaneously obtaining an improved resolution on the shape of the curve itself, the noise per-point increases. This method will employ a cadence (time between successive measurements) of 40sec as an example, but the `Github` code allows any cadence to be selected, thereby modifying σ_{pp}.

This provided a value of $\sigma_{pp} \approx 35ppm$, with the full curve shown in figure 16, with 'noisy' data for JWST sampled from the lightcurve with the surface volcano. The volcano has been modified to exhibit an $N_{ratio} = 1.0$ (see section 3.1.1) as this would have the greatest difference between models (see figure 28 (section A.5) for a model image). After a comparison has been performed the ratio can then be reduced if necessary. This figure also shows a lightcurve drawn from the limb-darkened model with no volcano, and this will act as the null hypothesis in section 3.6.

3.6. Monte-Carlo Simulations:

Now that noisy data has been replicated for the JWST, various models can be tested using a χ^2 fit to determine the significance that these models can be rejected. A method of performing a large number of samples with various models is the Markov Chain Monte Carlo (MCMC), which is Bayesian method of randomly sam-
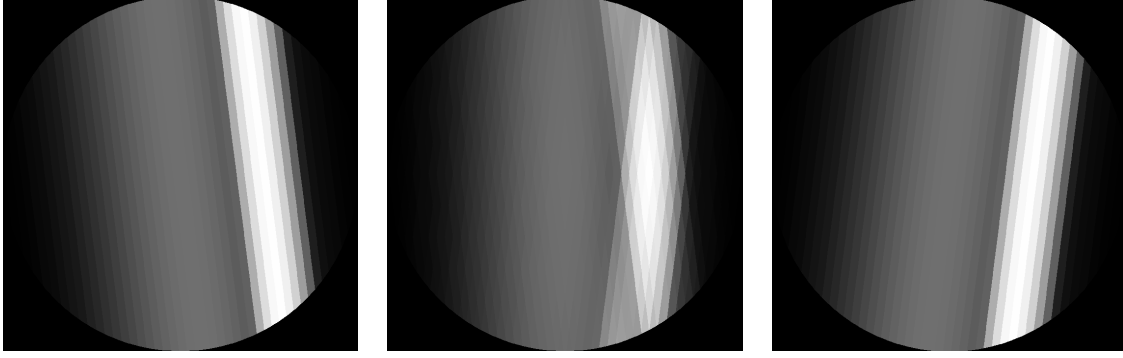
Figure 14: *Left: Reconstructed planet using the method in section 3.3 from only the ingress, with N_{slices} slices.*
Right: Reconstructed planet using only the egress, with N_{slices} slices.
Centre: Combined planet using both the ingress and egress sections, consisting of N_{slices}^2 slices.

Table 2: *Measurements and parameters for Spitzer and JWST, enabling a SNR for JWST to be calculated.*
Spitzer T1b Measurements from Triaud Private Communication (2017). Spitzer Diameter: Seager et al. (2009). JWST Area: Luger et al. (2017).

Parameter	Value
Spitzer Diameter	$0.85m$
Spitzer Area	$\approx 0.57m^2$
JWST Diameter	$\approx 5.64m$
JWST Area	$25m^2$
Spitzer Detection	$150 \pm 50ppm$
Spitzer SNR	3
No. Occultations	≈ 20
JWST SNR	≈ 20

pling a posterior probability distribution by adjusting various parameters (de Wit et al. (2012)). For example, if the 'limb-darkened' model (null hypothesis) with no features was modified and sampled with the volcano model noisy data, it would be possible to plot a posterior probability distribution (PPD) noting how the two models compare for the sampled parameters. If the 'limb-darkened' model had shifted by

a significant amount, the null hypothesis may be rejected, and a feature is detectable with a significance proportional to the error on the PPD.

This study has made use of a self-developed MCMC algorithm (also available on `Github`) which varies three parameters T_{tot}, T_{full} and ΔT. By examining figure 16 with the labelled parameters, it is predicted that the MCMC will simultaneously modify the null hypothesis model to match the volcano model using these parameters via:

1. T_{tot}, defined in equation (1). This is expected to be reduced as the flux of the planet is now concentrated into a smaller region.
2. T_{full}, defined in equation (2). Due to the concentrated flux, the planet will appear to be fully occulted for a longer duration.
3. ΔT (*midpoint*), the separation between transit and occultation, defined in equation (6). The red curve in figure 16 appears 'shifted' right, suggesting ΔT will increase.

The MCMC algorithm itself assumes a uniform prior on each parameter, with a burn-in of 10^4 samples and a main-run of 10^5 samples.
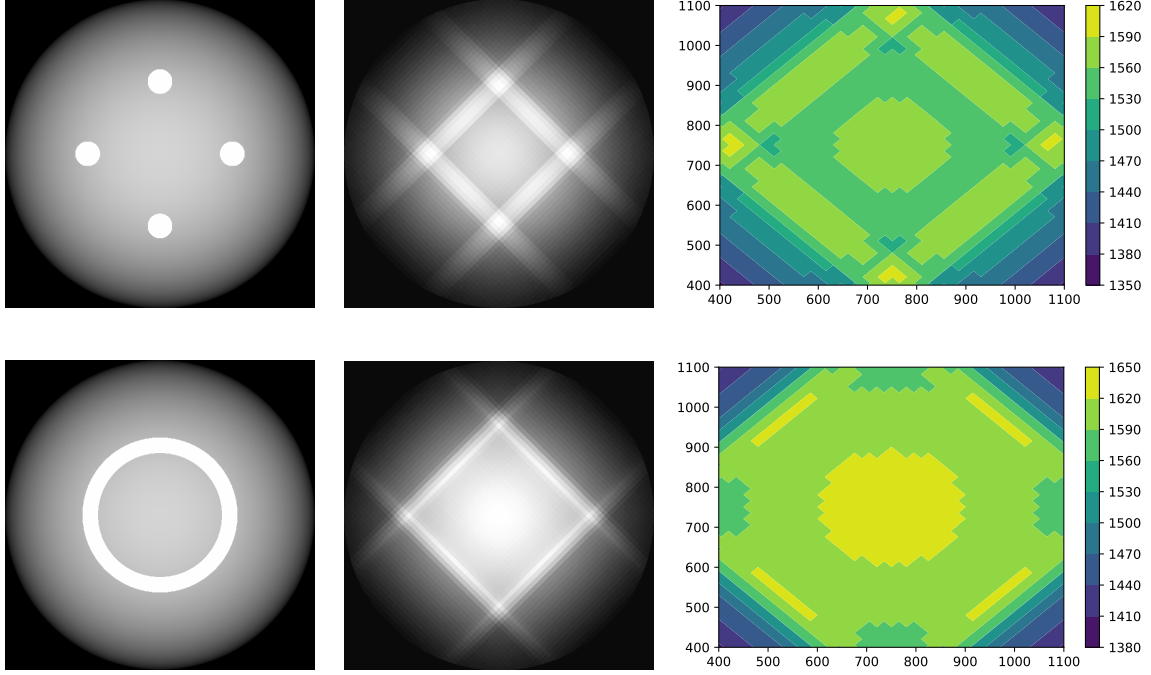
Figure 15: *Example pipeline showing (left-right) (a) an original model planet ($N_{slices} = 100$ chosen arbitrarily), (b) its reconstructed version and (c) a contour plot from the centre portion of each reconstructed image. Top row: Four surface features, each located $\frac{R_p}{2}$ from the centre, sliced at $\theta_{tangent} = \frac{\pi}{4}$. Bottom row: A continuous circular feature, also sliced at $\theta_{tangent} = \frac{\pi}{4}$.*

A lengthy burn-in was selected to ensure the starting conditions were 'forgotten' in the main sampling run (Gilks et al. (1995)). The limits for each prior in units of phase was chosen to be:

$$0.010 < T_{tot} < 0.020$$
$$0.010 < T_{full} < 0.020$$
$$0.490 < \Delta T < 0.510$$
$$T_{tot} > T_{full}$$

The first three originate from a visual inspection to limit the algorithm sampling too far from what is guessed to be an optimal solution, as the MCMC can take a considerable amount of time to complete. The latter stems from the physical requirement that the fully occulted time cannot extend beyond the total occultation time. With each sample, a new array of points is created (see section 3.2.1) and the null hypothesis model is re-drawn. At this stage, a χ^2 value is determined by calculating the vertical distance d from the lightcurve and the noisy JWST data utilising

$$\chi^2 = \frac{d^2}{\sigma_{pp}^2}, \tag{25}$$

where σ_{pp} is determined in section 3.5. This is converted to a probability (Andrae et al. (2010)) using

$$P\left(\chi^2\right) \propto e^{-\frac{\chi^2}{2}}, \tag{26}$$

where a proportionality has been used as only the relative probability of each sample is necessary, not the absolute value. The ratio of probabilities between the current and next sample,
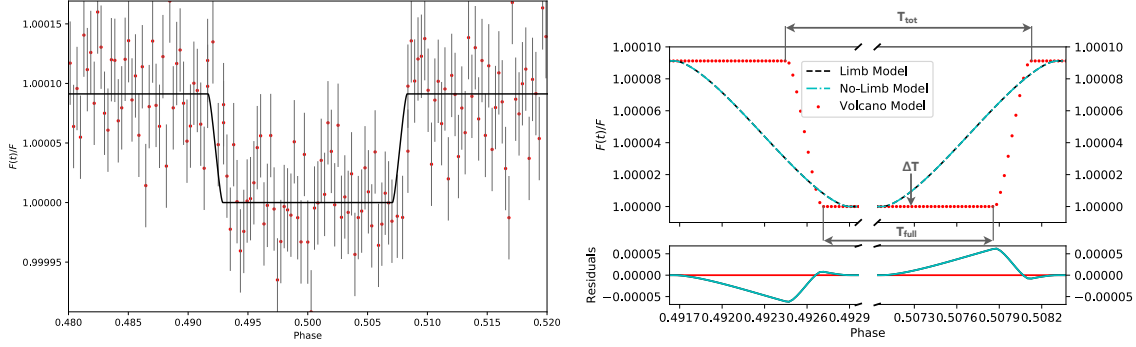
19

Figure 16: *Left: Example of noisy data using JWST SNR values from the volcano model. Each point has been randomly determined using Gaussian generator from the red curve in the 'right' image with a mean placed on the lightcurve and a standard-deviation from equation (24). The black curve is the null hypothesis which will be modified in the MCMC (section 3.6) to fit the noisy data.*

Right: Modified version of figure 12, with a volcano model utilising $N_{ratio} = 1.0$. Note there is a statistically significant difference between the volcano and non-volcano models, and this can be observed with the parameters T_{tot}, T_{full} and ΔT (midpoint).

$R = \frac{P_{n+1}}{P_n}$, is determined with the next sample position being accepted if $R > 1$. If $R < 1$, the sample may still be accepted depending on the Metropolis-Hastings (MH) algorithm (Gilks et al. (1995)), to prevent the MCMC becoming trapped in a local minima. An acceptance rate AR on the MH algorithm was optimised to ≈ 0.25 (Roberts et al. (2001), Sherlock & Roberts (2009)), with the step sizes for the three MCMC parameters being independently adjusted during the burn-in to reach this AR. The results from performing the MCMC is presenting in the results section 4.1.

3.7. Lifting Degeneracy:

It was observed by Knutson et al. (2007) that the Hot Jupiter HD189733b exhibits a time offset of ≈ 120 seconds (section 2.2), but it this is likely to not be the result of a non-uniform BD alone. By introducing an artificial BD to the planet's surface, an offset of 20 seconds was detected by Knutson, and so another cause

may be an eccentric orbit. Likewise any feature detection in section 3.6 due to the shift in MCMC parameters could also be a result of an eccentric orbit, and so this will be tested by examining how the equations in section 2.4 vary with eccentricity e and the argument of periapsis ω. By applying equation (6) for ΔT and equations (1) - (5) for T_{tot} and T_{full}, it is possible to observe this variation, with results presented in sections 4.2 (ΔT) and 4.3 (T_{tot} and T_{full}).

It can be predicted that the midpoint position will depend on ω, and this is visualised in figure 17. For $\omega = \frac{\pi}{2} = \frac{3\pi}{2}$, the time between when the two occurrences of the planet crossing the Z-axis (ΔT) will be exactly half an orbital period and the eccentricity of the orbit will have no impact on the midpoint measurements. However, if $\omega \neq \frac{n\pi}{2}$, the time between the planet crossing the Z-axis will appear shifted, and this will introduce a similar effect as the observation in section 3.6.
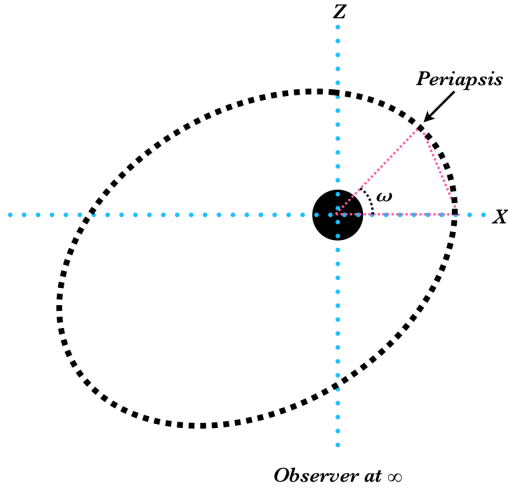
Figure 17: *Representation of how the argument of peri-apsis ω alters ΔT for an observer along the Z-axis for an eccentric orbit. This is measured between the two points of intersection (transit and occultation).*

4. RESULTS

4.1. Monte-Carlo Results:

After testing and building the MCMC algorithm, normalised histograms for the three sampling parameters can be found in figure 18 (two-dimensional versions in figure 30, section A.5). Asymmetric error ranges have been determined by plotting a skewed Gaussian using `"lmfit"` (Github), and finding the central region containing 68% of the total area. It can be seen that the three parameters have been modified as expected: T_{tot} has reduced, T_{full} has increased and the midpoint ΔT has increased. However, only ΔT lies $> 1\sigma$ from the original position, with the remaining parameters still residing within the 1σ asymmetric boundaries. It is therefore concluded that a shift in the occultation midpoint can infer a surface feature is present.

Along with the MCMC being analysed with

a single off-centered feature, the algorithm has also been tested with a central feature of equal size and flux ratio (see figure 29 section A.5), with the MCMC results presented in figure 19. The midpoint has not shifted due the feature residing in the centre of the model, but the other parameters now reside closer to the 1σ boundary. Whilst this is a small improvement over the results in figure 18, it does not constitute a significant detection. An additional test was performed by replacing the noisy volcano model data with the non-limb-darkened model to determine if the limb-darkening effect is significant enough to be detectable, with results presented in figure 32 (section A.5). The resulting 1σ confidence intervals are simple too large in this test that the two models cannot be distinguished.

4.2. ΔT (Midpoint) Degeneracy:

By plotting the variation of equation (6) in figure 20 (errors calculated in section A.3) using parameters from table 1, the $\cos(\omega)$ dependency becomes clear. As expected, any variation from $\omega = \frac{n\pi}{2}$ (for odd n) will cause the midpoint position to shift, and this exceeds the overlayed volcano result. The surface feature can only be detected in the range $\frac{\pi}{2} \lesssim \omega \lesssim \frac{3\pi}{2}$, as an eccentric orbit would decrease ΔT in this range.

Moreover, there is a possibility that an exoplanet with an eccentric orbit can also exhibit a non-uniform BD. In the event that the eccentricity of the orbit were known via a different source, such as radial velocity measurements (Winn et al. (2007)), it may be possible to measure the expected offset from this eccentric orbit which is created by a surface feature. This additional offset is presented in figure 21,
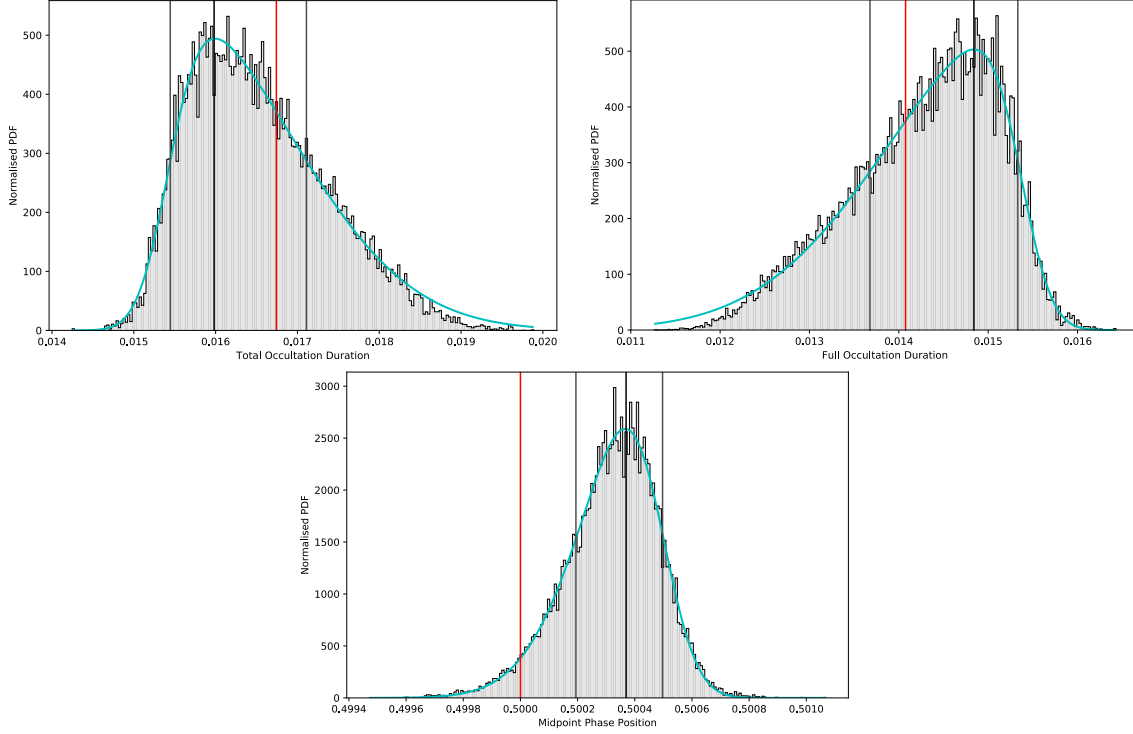
Figure 18: *Top-left: Normalised probability distribution function (PDF) histogram for T_{tot} with asymmetric errors plotted and a skewed Gaussian fit overlayed. Note the red line represents the null hypothesis starting position (black curve in figure 16).*
Top-right: Normalised PDF histogram for T_{full}.
Bottom: Normalised PDF histogram for ΔT (midpoint).

which shows the same eccentric offset from figure 20 and the combined eccentricity plus feature offset. For all values of ω, this additional offset lies $\approx 1\sigma$ from an eccentric orbit alone, suggesting that the null hypothesis of the feature detection originating from simply an eccentric orbit can only be rejected with $\approx 68\%$ confidence.

To expand on this, the separation between the variation in ΔT due to eccentricity alone and a combined eccentric plus volcano offset can be investigated further at $\omega = n\pi$ and $(n+1)\frac{\pi}{2}$, as the error varies between these two values. Specifically, for $n = 0$, the results are plotted in figure 22. From this, a dependency

is presented on ω:

- $\omega = n\pi$: An offset produced by eccentricity (with no added volcano) falls within the 1σ range of the additional volcano offset, suggesting that this degeneracy cannot be lifted.
- $\omega = (n+1)\frac{\pi}{2}$: The eccentric-only offset falls outside the 1σ range of the additional volcano offset, allowing for a 1σ detection to occur.

To confidently suggest a detection has taken place, it is often required that a 3σ separation must occur at 99% confidence. This would require $\approx 10\times$ the number of observed occultations to reduce the uncertainty to this level,
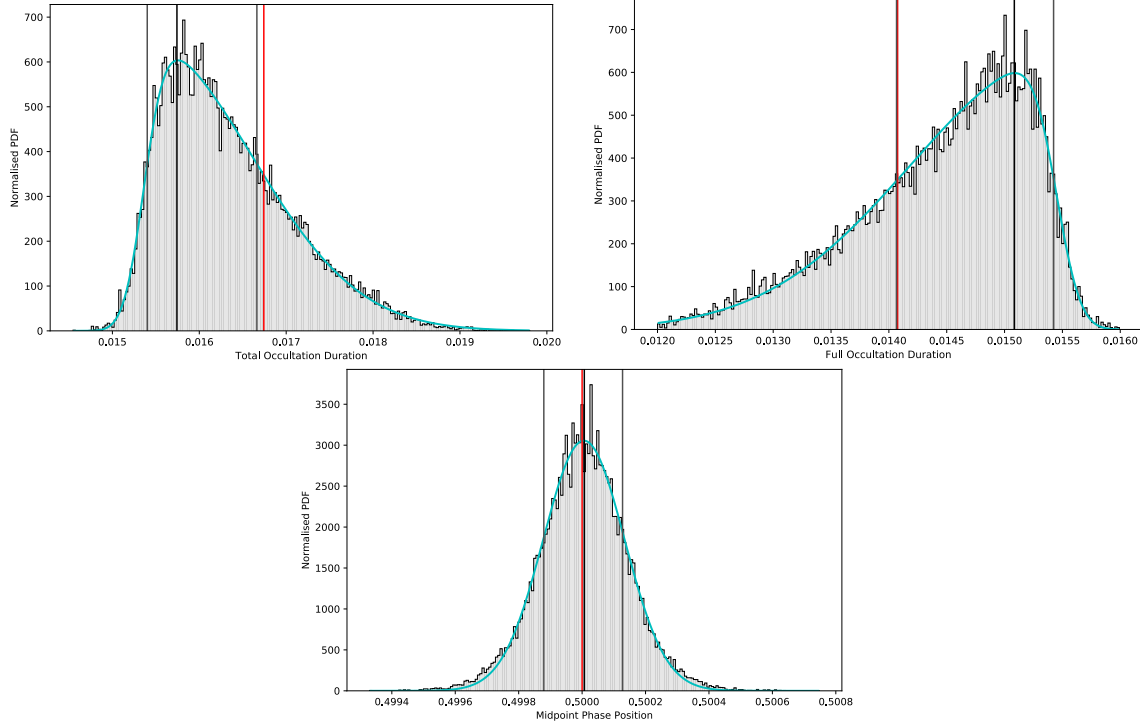
Figure 19: *Top-left: Normalised PDF histogram for T_{tot} with asymmetric errors plotted and a skewed Gaussian fit overlayed. Volcano position now resides in the centre of the model.*
Top-right: Normalised PDF histogram for T_{full}.
Bottom: Normalised PDF histogram for ΔT (midpoint).

necessitating 200 total occultations.

4.3. T_{tot} & T_{full} Degeneracy:

Along with the midpoint varying due to an eccentric orbit, the values of T_{tot} and T_{full} will also change. This is due to the exoplanet's orbital velocity varying throughout its non-circular orbit, depending on equations (1) - (5). This $e\sin(\omega)$ dependency is plotted in figures 23 and 24. It can be observed that the errors on the overlayed MCMC results are asymmetric from the mode value, and this stems from the asymmetry in figure 18. Furthermore, the 1σ MCMC results enclose almost all offset values that an eccentric orbit may introduce, therefore eliminating any possibility of lifting the

degeneracy regarding these two parameters. Errors were propagated via a Monte-Carlo for each parameter (see section A.3) in equations (1) - (5). The final parameters T_{tot} and T_{full} with errors can be determined and plotted as a histogram in figure 31 (section A.5), and was repeated for $\omega = \frac{n\pi}{2}$.

4.4. Other Results:

The estimation for the JWST SNR (section 3.5, table 2) relies upon 20 occultations, but it was discussed that the power output from a volcano would likely vary or dissipate entirely during this period. To estimate the telescope diameter necessary to obtain the same 1σ detection in only a single occultation, the noise
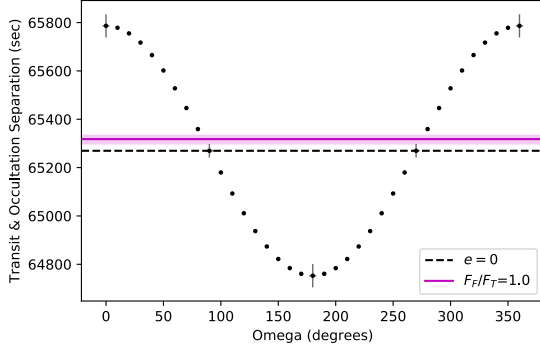
Figure 20: *Variation of ΔT using equation (6). Over-plotted is an equivalent midpoint shift due to a surface volcano with $N_{ratio} = 1.0$, and the value of ΔT for an orbit with no eccentricity. This volcano would cause ΔT to increase above the $e = 0$ line, but an eccentric orbit would create a larger impact for $\omega \lesssim \frac{\pi}{2}$ or $\omega \gtrsim \frac{3\pi}{2}$. Errors have only been plotted for $\omega = \frac{n\pi}{2}$ for readability.*

Figure 21: *Variation of ΔT due to:*
(a) an eccentric orbit alone (black).
(b) a combined eccentricity+feature offset (magenta).
Errors determined in figure 22 (see section A.3).

from Spitzer is multiplied by $(N_{occultations})^{\frac{1}{2}}$ to estimate the noise from one eclipse. This yields $SNR_{Spitzer} \approx 0.67$ and $SNR_{JWST} \approx 4.50$ using equation (23). To re-obtain the same SNR as used previously, an area of $\approx 500m^2$ (diameter $\approx 25m$) would be necessary. As the diameter of JWST ($\approx 5m$) is much smaller than this, a future project such as the ground-based Thirty Meter Telescope (Nelson & Sanders (2008)) may prove suitable, but this would introduce additional issues with the Earth's atmosphere which would require further consideration.

5. Discussion

By examining the results in section 4, it is clear that geolocating a volcano on a terrestrial planet is a difficult challenge and almost impossible using current technologies. Whilst past research has demonstrated that off-centred hotspots are present and observable on Hot
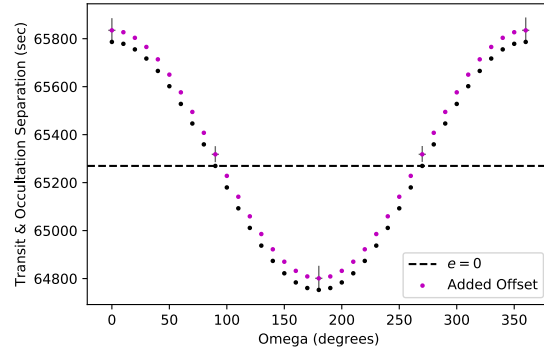
Jupiters, a terrestrial planet introduces additional difficulties. A terrestrial exoplanet is smaller than a gas giant, resulting in a reduced transit/occultation depth alongside a diminished SNR. Even by selecting a wavelength with a significant star-planet contrast to counteract this, a flux ratio $N_{ratio} = 1.0$ with optimistic T1 system errors in table 1 was necessary to produce a 2σ ΔT offset at 20 occultations for a circular orbit. For a different exoplanet system with a brighter star, the star-planet contrast may be worse than T1b and consequentially reduce the occultation depth, further impeding the detection of a surface feature. The circular assumption may be flawed as tidal disruptions can be generated by an eccentric orbit (see section 2.3), and it has been found that lifting the degeneracy with eccentricity can only be achieved to a 1σ significance, which also depends on the argument of periapsis ω. The other MCMC parameters T_{tot} and T_{full} cannot be employed in lifting this degeneracy due to their increased error values, with the MCMC
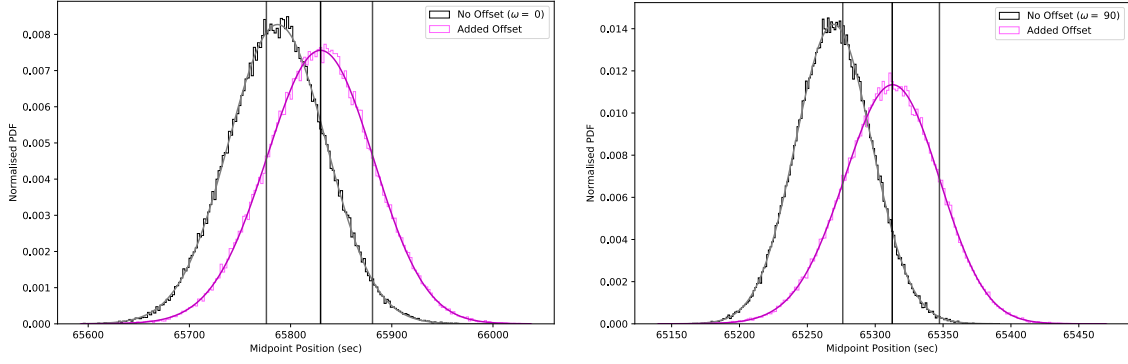
Figure 22: *Monte-Carlo error simulations of figure 21 for $\omega = 0$ (left) and $\frac{\pi}{2}$ (right). Each plot displays a normalised ΔT histogram for an eccentric orbit and with an additional offset due to the surface volcano, along with a skewed Gaussian fit and 1σ confidence interval.*
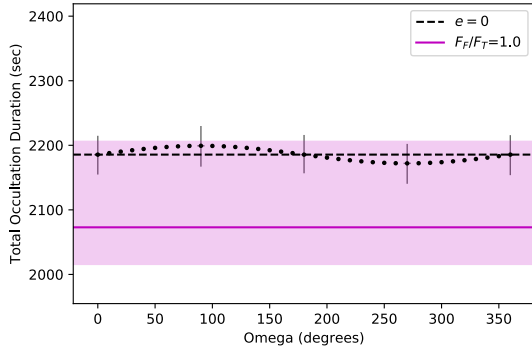

Figure 23: *Variation of T_{tot} due to an eccentric orbit. Overplotted is the MCMC result for a surface volcano with $N_{ratio} = 1.0$. Errors have been estimated via a Monte-Carlo simulation.*
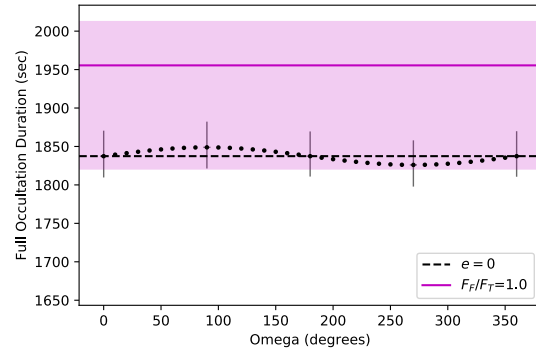
Figure 24: *Variation of T_{full} due to an eccentric orbit, along with the MCMC surface volcano result. Errors have been estimated via a Monte-Carlo simulation.*

results enclosing all possible values due to an eccentric orbit. This was suggested by Winn (2010), stating that often $e\cos(\omega)$ is constrained more powerfully than $e\sin(\omega)$.

Observing a planet with a volcano exhibiting 100% of the surface flux is unlikely, and so realistic results would only worsen when compared to those presented in this study. It was stated in section 4 that 200 occultations may shift the detection of a surface feature alongside an eccentric orbit to 3σ, but this opposes the requirement that the smallest possi-

ble number of observations is preferable due to the rapid variability of surface volcanoes (de Kleer & de Pater (2016)). It is therefore suggested that the eclipse mapping technique is only viable for permanent or long-lasting surface features, such as a magma ocean. Despite this possibility, magma is unlikely to exhibit such a large brightness distribution which has been employed here, suggesting the next step contributing to this research would be to test varying values of N_{ratio} and feature arrangements to determine the lowest possible ratio

25

which would still produce a $> 1\sigma$ detection. Some arrangements can introduce degeneracy in the final reconstructed image (section 3.4), with only two specific cases having been examined in this study. These degenerate cases may change if the linear assumption in section 3.1.2 is removed, which is important for larger planets or even gas giants with radii much larger than terrestrial planets, with curved slicing observed by Majeau et al. (2012). It is therefore an ideal route of investigation to reapply the methods developed within this study to a variety of exoplanet systems with curved slicing to determine how the reconstructed images differ.

As discussed in section 2.2, de Wit et al. (2012) investigated the effect of assuming HD189733b as a uniformly-bright disk and Rauscher et al. (2007) implemented limb-darkening by varying the surface temperature of the planet. The results presented in section 4 and figure 32 (section A.5) suggest that a limb-darkened and uniformly-bright planet cannot be discerned with the accuracy of JWST to at least 1σ significance. Hence it was not unreasonable for past research to assume uniformly-bright disks when modelling exoplanets, and changing the null hypothesis in this study when comparing to the volcano model may have minimal impact. However, it was discovered by de Wit et al. (2012) that the conventional assumption of a uniform BD can result in underestimated uncertainties on system parameters due to their correlation if the data is of sufficient quality. It is therefore a possible line of investigation to determine if any particular volcano arrangements or limb-darkening effects introduce a significant difference between the two possible null-hypotheses.

6. CONCLUSION

Eclipse mapping is a powerful technique which can extract two-dimensional spatial information from a lightcurve which would traditionally only measure a disk-integrated value. By applying this technique to other worlds, photospheric emission models can be differentiated, time offsets from an expected occultation can be detected and the positions of hotspots can be inferred. This study has applied research from gas giants to a transiting terrestrial planet to determine if a volcanic hotspot would be detectable and examined the issues which may arise. A transiting planet is likely to be eclipsed by its host star, unless it exhibits a significantly eccentric orbit. A simulated occultation for T1b was developed from first-principles and applied to three model planets, two with varying levels of limb-darkening and one with an additional surface volcano. By linearly slicing the image at an angle depending on the orbital impact parameter and assuming a circular orbit, a lightcurve was generated and modelled using various system parameters. An image was then reconstructed from the volcano model lightcurve by splitting the curve into segments and averaging the variation in flux between slices across a segment of the planet. Degenerate examples were also tested to discover a method of discerning visually similar reconstructions.

To determine the significance that the reconstructed images can be separated from a null hypothesis model with no volcano, noisy data was simulated for the JWST with an estimated SNR of ≈ 20 for a volcano exhibiting 100% of the planet's flux with 20 occultations. By modifying the three parameters that can alter the shape of a lightcurve, a 2σ shift was

found for ΔT. By shifting the volcano's position to the centre of the planet, T_{tot} and T_{full} were instead shifted by 1σ. By testing if these properties can be observed if the orbit were non-circular, a 1σ ΔT detection was found to be possible, requiring ≈ 200 occultations to reach 3σ. Furthermore, a telescope with a diameter $\approx 25m$ is necessary to detect a similar shift in only a single occultation, with such a detection remaining seemingly impossible in the near-future. It has also been found that the assumption of a planet exhibiting a BD of a uniformly-bright disk is not unreasonable, but it is also noted that this assumption can underestimate uncertainties due to the correlation with other exoplanet parameters, and hence all analyses has been performed with the limb-darkened model. It is therefore concluded that geolocating a volcano on an extrasolar planet is challenging but not impossible, with longer-lasting features detectable if unchanged over 200 occultations. This study has also developed the simulations necessary to apply this research to additional exoplanet systems with varying surface features, allowing future investigations to build upon these results.

References

Andrae, R., Schulze-Hartung, T., & Melchior, P. 2010

Ciardi, D. R., Yee, J. C., Ballard, S., et al. 2017, The Science Case for an Extended Spitzer Mission, 8

de Kleer, K. & de Pater, I. 2016, Icarus, 280, 378

de Kort, J. J. M. A. 1954, Ricerche Astronomiche, 3

de Wit, J. 2014, PhD thesis, Massachusetts Institute of Technology

de Wit, J., Gillon, M., Demory, B.-O., & Seager, S. 2012, A&A, 548, A128

Gaidos, E. J. & Nimmo, F. 2000, Nature, 405, 637

Gilks, W. R., Richardson, S., & Spiegelhalter, D. 1995, Markov chain Monte Carlo in practice (CRC press)

Gillon, M., Triaud, A. H., Demory, B.-O., et al. 2017, Nature, 542, 456

Grimm, S. L., Carey, S., & Ingalls, J. G. 2018, A&A

Kislyakova, K., Noack, L., Johnstone, C., et al. 2017, Nature Astronomy, 1, 878

Knutson, H. A., Charbonneau, D., Allen, L. E., et al. 2007, Nature, 447, 183

Lindsey, J. 2018, School of Physics and Astronomy, University of Birmingham

Luger, R., Lustig-Yaeger, J., & Agol, E. 2017, ApJ, 851, 94

Majeau, C., Agol, E., & Cowan, N. B. 2012, ApJ Letters, 747, L20

Murray, C. & Correia, A. 2010, Exoplanets, 15

Nelson, J. & Sanders, G. H. 2008, in Ground-based and Airborne Telescopes II, Vol. 7012, International Society for Optics and Photonics, 70121A

Rauscher, E., Menou, K., Seager, S., et al. 2007, ApJ, 664, 1199

Roberts, G. O., Rosenthal, J. S., et al. 2001, Statistical science, 16, 351

Seager, S. & Deming, D. 2010, Annual Review of A&A, 48, 631

Seager, S., Deming, D., & Valenti, J. 2009, in Astrophysics in the Next Decade (Springer), 123–145

Sherlock, C. & Roberts, G. 2009, Bernoulli, 774

Stephens, G. L., Li, J., Wild, M., et al. 2012, Nature Geoscience, 5, 691

Williams, P. K., Charbonneau, D., Cooper, C. S., Showman, A. P., & Fortney, J. J. 2006, ApJ, 649, 1020

Winn, J. N. 2010, Exoplanets, 55

Winn, J. N., Holman, M. J., Henry, G. W., et al. 2007, The Astronomical Journal, 133, 1828

A. Appendix

A.1. Slicing Coordinates:

The $(x(n), y(n))$ coordinates for each slice position in figure 9 can be determined via

$$x(n) = (n+1) \times L_{slice} \times \cos(\theta_3) \quad (27)$$
$$y(n) = (n+1) \times L_{slice} \times \sin(\theta_3), \quad (28)$$

where n is the slice number, ranging from 0 to N_{slices}. Note that $(n+1)$ is used in these equations as the Python loop begins at $n = 0$. By using the (x, y) coordinates to determine each *"Slicing Position"* in section 3.1.2, the slices themselves can be plotted, with an example in figure 27 (section A.5). The slices themselves are drawn between $[x_{min}(n), x_{max}(n)]$ and $[y_{min}(n), y_{max}(n)]$. These maximum/minimum values must lie beyond the boundaries of the planet's two-dimensional array, and are

$$[x_{slice,min}, x_{slice,max}] = [x(n) - C \times \cos(\theta_{tangent})$$
$$, x(n) + C \times \cos(\theta_{tangent})] \quad (29)$$

for x, where C is an arbitrary length such that the slicing lines will always traverse the entire image. The equivalent values in y are

$$[y_{slice,min}, y_{slice,max}] = [y(n) - C \times \sin(\theta_{tangent})$$
$$, y(n) + C \times \sin(\theta_{tangent})]. \quad (30)$$

This enables ingress/egress slices to be simulated for any exoplanet system with the linear slicing algorithm at any angle.

A.2. Verifying the Model:

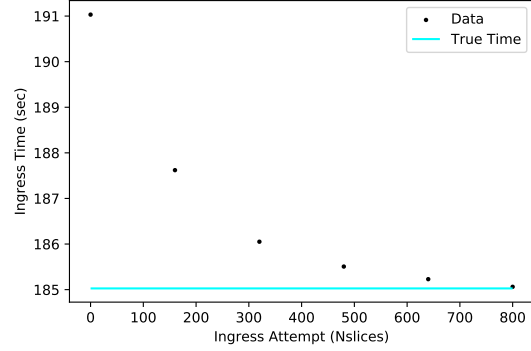To verify whether the model replicates timing from the T1b system, the slicing algorithm in

Figure 25: *Plot of model ingress time t_{model} dependence on N_{slices}. The "true time" is determined using equation (3).*

section 3.1.2 can be tested to ensure the simulated ingress/egress time matches the true value. This can be accomplished by noting that not all slices within figure 9 encompass the planet, and so by measuring the distance across all slices which do contain some region of the planet, its 'diameter' can be calculated in units of L_{slice}. Furthermore, if the horizontal velocity of the planet is known, the ingress/egress time can be found and compared to the true value.

Before this can be concluded, a conversion factor between SI units (metres) and model units (pixels) must be found. This is simply written as

$$CF = \frac{2 \times R_P}{X} \left[= \frac{[m]}{[pix]} \right], \quad (31)$$

where R_P is the planetary radius and X is the X-dimension of the model planet. As the planet spans the entire X-dimension in figure 9, it is exactly equal to the planet's diameter. From this, the ingress/egress time can be computed using

$$t_{model} = (n_{final} - n_{initial}) \times CF \times \frac{L_{slice}}{V_{P,slice}}, \quad (32)$$

29

where n is the slice number and $V_{P,slice}$ is the planetary slicing velocity. The value of $V_{P,slice}$ must be modified from the simple orbital velocity V_P, however, as the slicing does not occur vertically. This is defined as

$$V_{P,slice} = V_P \cos(\theta_3), \qquad (33)$$

with θ_3 presented in figure 9. This translates the orbital velocity in the X-axis to the *"Coordinate Line"*. A resulting plot of t_{model} is shown in figure 25 as a function of N_{slices}. It can be observed that the algorithm slightly overestimates t_{model} by $\approx 6sec$ initially, which exponentially approaches the true value. This is caused by the L_{slice} decreasing as N_{slice} increases, which will increase the measurement accuracy of the planetary diameter in units of L_{slice}. Therefore, for 50 slices, the model uncertainty is $< 5sec$, and can be reduced to almost zero at ≈ 800 slices.

A.3.   Error Calculation:

To propagate any errors without asymmetric error boundaries, the general equation for a parameter f depending on parameters x_i can be found using:

$$\sigma_f^2 = \Sigma_{i=1}^N \left(\frac{\partial f}{\partial x_i} \right)^2 \sigma_{x_i}^2, \qquad (34)$$

where N is the total number of parameters and σ is the standard deviation. This assumes the parameters are independent and neglects any correlations.

In the case that 1σ error values are asymmetric, the error can either be propagated using the higher error boundary or a Monte-Carlo simulation can be applied, which is the case in sections 4.2 and 4.3. This generates arrays of 10^5 samples for each parameter with mathematical operations being performed on these to create a final array for the parameter of interest. As presented in the example figure 22, the final array can be fitted with a skewed Gaussian to determine the central 68% confidence region, allowing asymmetric errors to be extracted.

A.4.   Unsuccessful Methods & Issues:

The majority of time devoted to this study was spent generating the model simulation to replicate the T1b system and creating the MCMC algorithm to extract the necessary results. As with any form of research, some methods were unsuccessful and abandoned, which include:

1. The MCMC originally only employed two parameters, ΔT (midpoint) and T (time between mid-ingress and mid-egress.) A third parameter was only added towards the end of the project when it became clear that the MCMC was not correctly determining the optimal shift to the null hypothesis. This was discovered when the modal values from the MCMC were plotted and the curve did not align with the volcano model in figure 16. It was then thought that modifying the ingress/egress time would correct this, and so T was replaced with T_{tot} and T_{full}, which then did align with the volcano model.

2. The plots in figure 31, which demonstrate how the errors on T_{tot} and T_{full} were found using a Monte-Carlo simulation, are not a true fit to the skewed Gaussian model. This can be observed at the peak and edges of the curves. Due to time constraints this has not been rectified, and the 1σ boundaries were still determined using this method. However, given additional time, this would require further investigation to determine a curve-fitting algorithm

to overcome this challenge.

3. The occultation direction in section 3.1.2 currently assumes the planet occults in the negative X-direction (counter-clockwise) and this cannot be easily modified in the code. To simulate a planet orbiting in the opposite direction, the ingress/egress reconstructions in figure 14 can be swapped to correct for this.

4. Equation (5) is only approximate, with an accurate version provided in equation (7) by de Kort (1954). By taking the approximation $\tan^{-1}(x) \approx x$, the additional $O\left(x^3\right)$ term has been neglected due to its dependence on e^3, which is a very small value.

A.5. Plots & Figures:
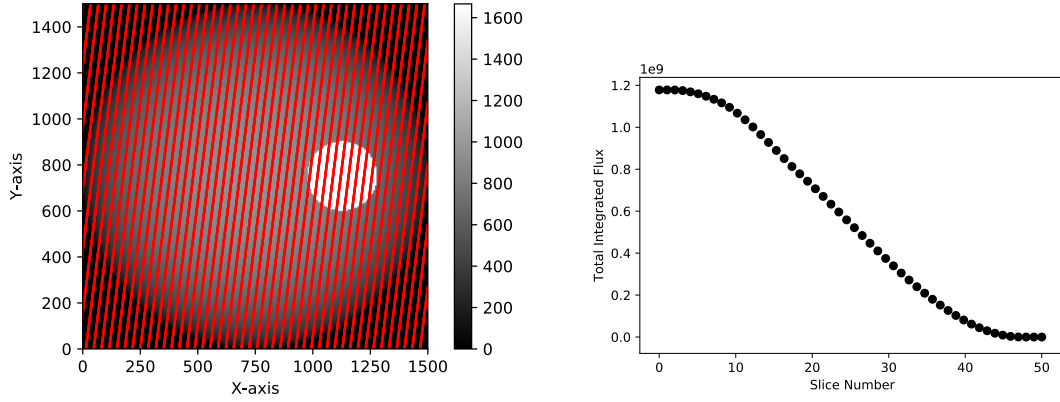
Figure 26: *Result of the slicing method described in section 3.1.2. Left: egress phase. Right: resultant lightcurve. The lightcurve is simulated by progressively reapplying individual slices from the segmented model. Each slice is reapplied to the total integrated flux to replicate a planet re-emerging from a secondary eclipse. Note the lightcurve appears to be an ingress, but this is reversed when plotted in figure 12.*
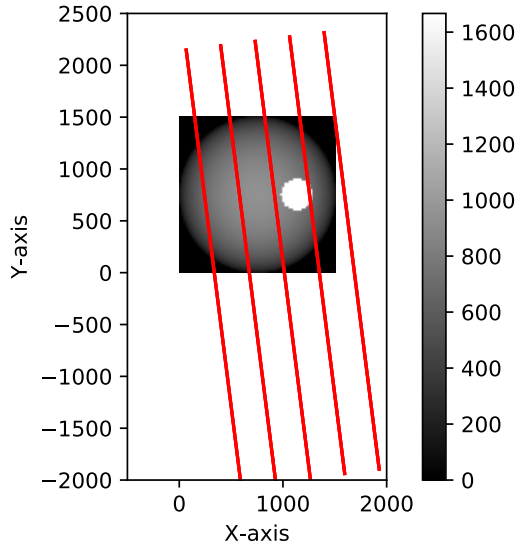

Figure 27: *Example of ingress slicing figure 10 without limits imposed, with $N_{slices} = 5$ for simplicity. Starting from $(0, 0)$, five lines can be observed, slicing the image into five segments. The final line can be ignored and is plotted to test if the algorithm correctly placed the last slice in the upper-right corner. These lines exceed the border of the image, with has no impact on the final algorithm.*
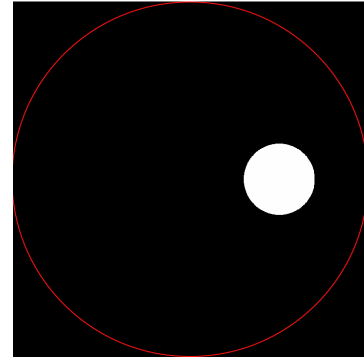

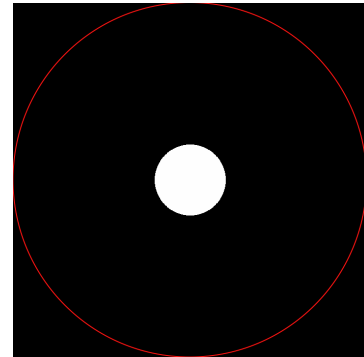**Figure 28:** *Modified model planet from figure 6 with $N_{ratio} = 1.0$.*

Figure 29: *Modified model planet from figure 6 with $N_{ratio} = 1.0$ and the volcano shifted to the centre.*
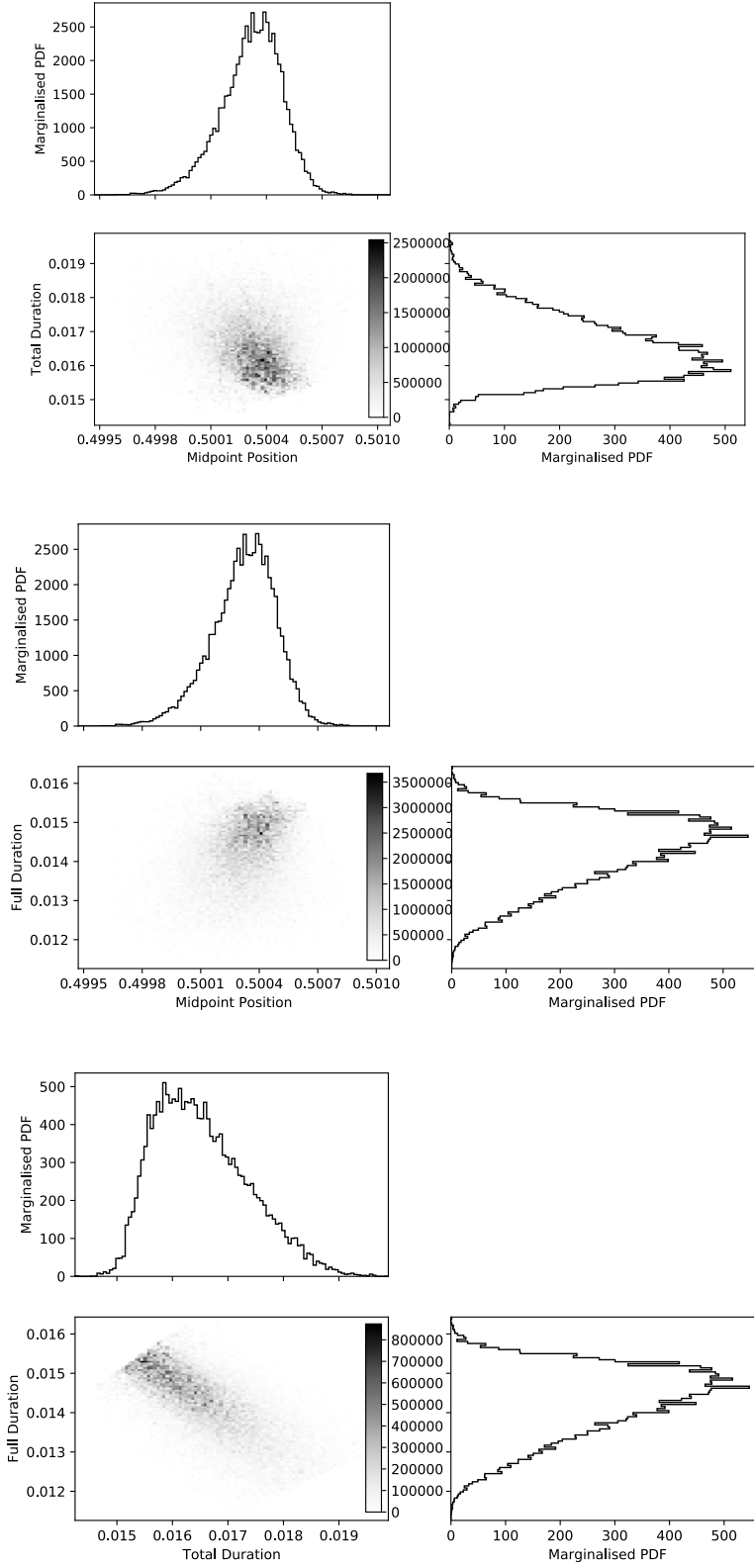
Figure 30: *Two-dimensional normalised histogram PDF plots relating the three MCMC parameters in figure 18. All non-PDF axes are in units of orbital phase. Note the 'barrier' in the bottom two-dimensional plot relating the total and full duration is due to the prior stating $T_{tot} > T_{full}$.*

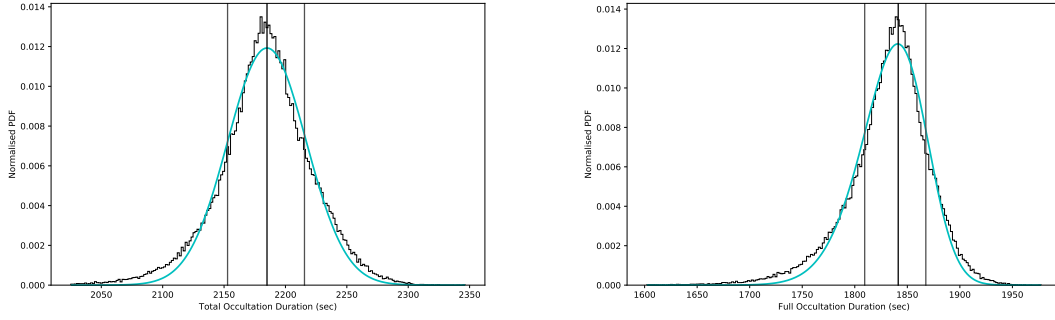**Figure 31:** *Normalised histogram results for T_{tot} (left) and T_{full} (right) via a Monte-Carlo simulation of 10^5 random samples. A skewed Gaussian model has been fitted to allow the 1σ interval ranges to be determined.*
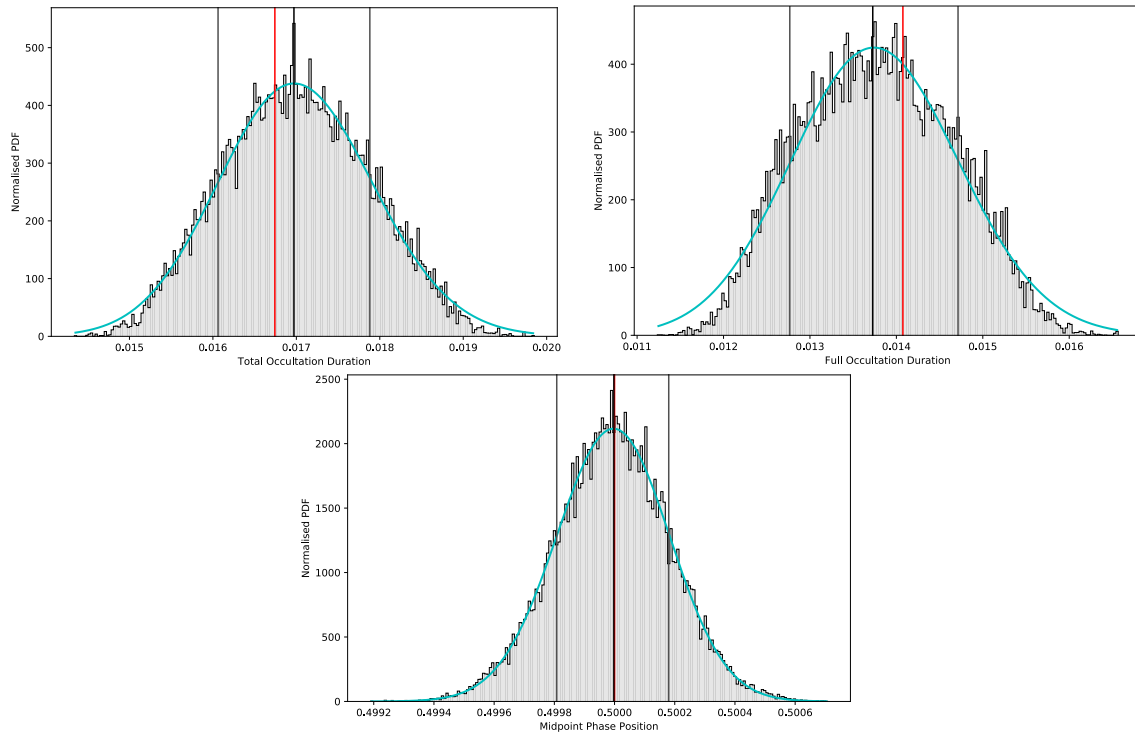

Figure 32: *Top-left: Normalised PDF histogram for T_{tot} with asymmetric errors plotted and a skewed Gaussian fit overlayed. Noisy data is now generated from the non-limb-darkened model with the limb-darkened planet acting as the null hypothesis.*
Top-right: Normalised PDF histogram for T_{full}.
Bottom: Normalised PDF histogram for ΔT (midpoint).